

Multi-band bathymetry mapping with spiking neuron anomaly detection

J. LAWEN¹, K. LAWEN², G. SALMAN³, AND A. SCHUSTER³

¹*Institute of Process Systems Engineering, Hamburg University of Technology, Am Schwarzenberg-Campus 4 (C), Hamburg, 21073*

²*Nvidia, 2788 San Tomas Expressway Santa Clara, CA 95051*

³*Department of Computer Science, Technion - Israel Institute of Technology, Israel*

* Corresponding author: jl@environment.report

Compiled February 22, 2022

The developed method extracts bathymetry distributions from satellite images, processing one, two or three of the common RGB bands. The remote sensing is sparsely coded and combines spiking neural net anomaly filtration, spline and multiband fitting. Survey data were used to identify an activation threshold, decay rate, spline fittings and multi band weighing factors. Errors were computed for remotely sensing Landsat satellite images. Multiband fittings achieved an average error of 26 cm. This proved sufficiently accurate to also automatically extract shorelines to eliminate land areas in bathymetry mapping. © 2022

Johannes Lawen

<http://dx.doi.org/10.1364/ao.XX.XXXXXX>

1. INTRODUCTION

Bathymetry, that is underwater topography, exhibits a depth dependent correlation with pixel shadings in satellite imagery. Remote estimations of water depths have been particularly successful for shallow waters with detectable reflections from the seafloor. Absent atmospheric correction, machine learning has been found to be superior over fittings to rigorous optical models [1]. Neural nets have been extensively used for remote sensing, including convolutional neural nets, NN-physics hybrid methods [2], and to utilize multiple bands or spectra [3].

The remote sensing has to account for uneven numbers of measurements per pixel, shared pixel shadings for a measured depth, different measured depths for the same shading, different fittings for different bands, and simply anomalies on: 1) the seafloor due to vegetation, varying geology or anthropogenic effects such as pollution and 2) instances of cloud cover besides gradual atmospheric interference. The uncertainty in littoral waters has been estimated at 0.39 m [4] which is in this work contrasted with an average of 0.21 m.

Spiking neural nets have found application in anomaly detection for time series [5] and image processing [6]. In this work spiking neural nets are used to detect anomalies in bathymetric data. The developed solution comprises a spline fitting, spiking neuron (SN) anomaly detection, and multi-band fitting. Whereas neural nets are stationary, spiking neurons introduce a differential regime with activation functions that exhibit decays between successive stimuli. The decay occurs usually along time but can also occur along a spatial dimension.

The latter has been utilized here, harnessing the SNN to filter

outliers. That is, the differential between a local depth value and proximate values, weighted by its reciprocal distance, is used to stimulate activation. Each stimuli is followed by exponential decay. Dynamic SNN permit to integrate a growing set of data into a binary decision of in- or excluding data. This is an important feature to permit the onward development of remote sensing based on multi-temporal satellite images [7, 8]. The SNN is sandwiched between a pre- and post-processing that can be formulated in either fashion: the pre-processing can be denoted as a spline fit followed by the computation of the SN-input or as a classical sparse neural net. Likewise, the post-processing can be denoted as a weighted linear fitting or as a classical neural net.

For bathymetry estimations the use of three RGB bands was found to return more robust results than using one or two bands alone [1]. More robust means here that whereas monochrome sensing failed for some pixels (Figure 3), multi-band sensing returned estimates for all pixels. An open source Landsat 8 image from the USGS Earth Explorer [9], has been used. Band values that turn out unsampled in the survey or share the same depth received an interpolated allocation. Anomalies were mitigated with the spiking neuron layer. Stationary data were made compatible with the transient functioning of SNN by substituting time with the radius around a pixel that is being processed. The threshold for the spiking neurons has been identified iteratively until either the sensing error was minimized or features, such as shores and highways, were extracted best — depending on the task. Figure 3 shows the extracted bathymetry surrounding south Bahrain and the artificial islands at the island's eastern coast.

2. METHOD

Outlying pixels are filtered with spiking neurons by converting the neuron's transient dependency to a spatial one. A spiking neural net (SNN) mirrors natural neural nets by obeying exponential decay of stimuli. Spiking neurons are reset once accumulating stimuli pass the neurons' thresholds. Outlying soundings or depths can be filtered versus the sorted measurement series or the seafloor background. In this paper the filtration occurs vs. the seafloor background which will allow usage also for noise filtration in other image types. That is, if a depth magnitude is not re-stimulated with increasing distance r and reciprocal weight, then it falls below the threshold with the activation function f .

$$f(r_j^+) = f(r_j^-) + \sum_{\forall d^*(r_j)} \frac{|d_i^* - d^*(r_j)|}{r_j d_i^*} \quad (1)$$

$$f(r_j + \delta r_j) = e^{-\delta r_j} f(r_j) \quad (2)$$

where the input is the cumulative discrepancy between the input depth d^* at a particular location i and the depths at a neighbor location r_j until the cutoff radius r_{cutoff} . The distance of locally proximate centroids, r_j , is obtained in sorted order with $r_j = \sqrt{a_j^2 + b_j^2}$ with $a_0 = 0$,

$$a_j = a_{j-1} + 0^{b_j} \quad (3)$$

where a_j and b_j are the radius' vertical and horizontal component respectively.

$$b_j = \quad (4)$$

$$\left((a_{j-1} + 1) \left(1 - \frac{a_{j-1} \bmod 2}{2} \right) + n \right) \bmod (a_{j-1} + 1)$$

Eq. 3 was obtained by observing that a_j increments whenever b_j resets to zero. a_j equals the growth period of b_j and the growth height b_j . Hence, b_j can be constructed out of a mutual reference of the two quantities and the index j : When b_j vanishes, then the recursive sequence shown in Eq. 3 exhibits a leap of one unit length. When b_j returns any other natural number, then series Equation 3 remains constant. Hence, using the recursive series b_j in the exponent of 0, permits to obtain the recursive series a_j . I.e., as b_j is alternating between a natural number and 0, a_j alternates between growth and stagnation.

The code for Eq. 2 and 3 are provided with the code for the neural net as link in the appendix. Alternatively, a_j can also be obtained by incrementally summing the elements of the lower triangle matrix of the identity matrix with ascending indices.

$$a_{1+p(p+1)/2+q} = \sum_{p=0}^j \sum_{q=0}^p I_{pq} \quad (5)$$

Matrix storage can be omitted by denoting the identity matrix implicitly as exponent of 0 to the power of the difference of its indices:

$$a_{1+p/2(p+1)+q} = \sum_{p=0}^j \sum_{q=0}^p 0^{p-q} \quad (6)$$

The code for Eq. 6 is provided in the Appendix such that a_j is obtained readily sorted. As a third alternative, the same series has been recovered with an analysis based on Theorem ?? and 6 in the appendix.

If the entire processing is supposed to be integrated into one

neural net, then the computation of the input for the spiking neurons can be formulated as arithmetic neurons [10] which are fed by neurons which conduct a spline fit. Prior to the spline fit routine, survey data are curated by removing all soundings above the water surface. The pre-processing prior to identifying the neuron properties is conducted, hence, by eliminating all dry measurements m .

$$m = m^* (\forall m^* > 0) \quad (7)$$

An input quantity is differentiated from an output quantity by indication of a superscript asterisk. Measurements m , i.e. echo soundings, are then correlated with satellite image values v according to

$$\sum_{\forall dim} |x_{dim}^m - x_{dim}^v| \Big|_{min} \quad (8)$$

for the distance x . Given the satellite image resolution of 30 m , measurements that share a pixel are averaged. Measurements that share the same pixel shade are averaged too. Associated measurements and pixel shades are bookkept by referencing for a particular post-processing measurement the found post-processing pixel shading in the second layer. This is conducted for each color or band. The third layer, the arithmetic neurons compute the input term in equation 1. The SNN layer then processes the output depths further as per equations 1, 2, and

$$d = d^* (\forall f < f_{th}) \quad (9)$$

with the threshold f_{th} . Pixels where the successive weighted deviations pass the threshold are deemed outlying and eliminated. The multiband fitting then utilizes some unused echo measurement values to compute the best band weighting factor $w_{ic} \in \mathbf{w}_i$ for a particular color c and pixel shading. The nonzero values for a particular vector \mathbf{w}_i of weighing factors are, hence, given with

$$\begin{aligned} w(d_c^*|_{min}) &= 1, & \text{for } d^m < d_c^*|_{min} \\ w(d_c^*|_{max}) &= 1, & \text{for } d^m > d_c^*|_{max} \\ w_a &= \frac{d^m - d_b}{d_a - d_b} \wedge \begin{bmatrix} a \\ b \end{bmatrix} = \mathbf{c}(\notin d_c|_{max}), & \text{for } \frac{c(d^m > d_c^*)}{c(d^m > d_c^*)} = 2 \\ \wedge w_b &= \frac{d^m - d_a}{d_b - d_a} \wedge \begin{bmatrix} a \\ b \end{bmatrix} = \mathbf{c}(\notin d_c|_{min}), & \text{for } \frac{c(d^m < d_c^*)}{c(d^m < d_c^*)} = 2 \end{aligned} \quad (10)$$

for a particular pixel i and colors $[a \ b \ c]$. Equations 10 merely describe the different cases of weighting two adjacent depths out of three band estimates to return the measured depth. If the measured depth is above or below the highest and deepest estimate respectively, then only one band is used. If the measured depth lays between the first two or the last two of the three bands, then the former or the latter are picked to contribute to the weighting. Hence, equations 10 contain four cases.

Hence, assuming that all processing is to be cast into one neural net: whereas the synapses between the first and second layer conduct merely a spline fit, the multi-band fitting post SN works like a bona fide neural layer where several inputs vote with individual weighting factors.

The intersected SN layer permits to exclude locally volatile pixel values which entail a high probable error. The functioning of a spiking neuron and particularly the circle-shaped arithmetic stimuli input is illustrated in Figure 1 below.

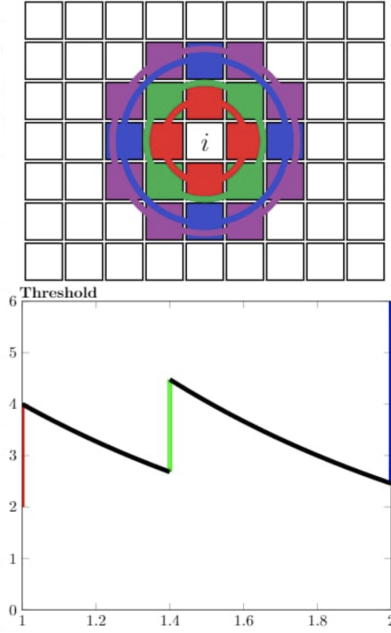


Fig. 1. With discrete circle slices incrementally more remote neighbors are compared to any examined centroid pixel, precluding anomalies.

The quantities that determine the size of the neural layers are listed in Table 1 below.

Table 1. Size quantities

Quantity	Pixel Property	Case
p	$2^{bit\ depth}$	2^{16}
r	$depth_{max} \times resolution / [m]$	16.5×10^2
e	horizontal number	7,631
v	vertical number	7,781
l	locally proximate: $1 + 3 \times 2^2 + 2^3 + \dots$	here:21

Increasing spatial distance corresponds in this artificial SNN to increasingly delayed time of stimulation. The refinement of this conversion might warrant to examine the conversion of still perception fields to transience in biological SNN and if this exploits the difference in transmission times of chemical vs. electrical synapses. Based on parameter estimation iterations, the threshold of the neurons is set to 6 for error filtration. The error is computed based on a comparison between the sensed prediction and one third of the soundings that are retained to quantify the method's accuracy. That is, the first third is used to conduct the spline fitting for all bands, the second third is used to assess the spline fittings' errors before and after spiking neuron filtration and to conduct the weighting of bands, the remaining third is used to estimate the error of the composite fitting before and after spiking neuron filtration. The function

of the normal, arithmetic and spiking layers are illustrated in Figure 2 below.

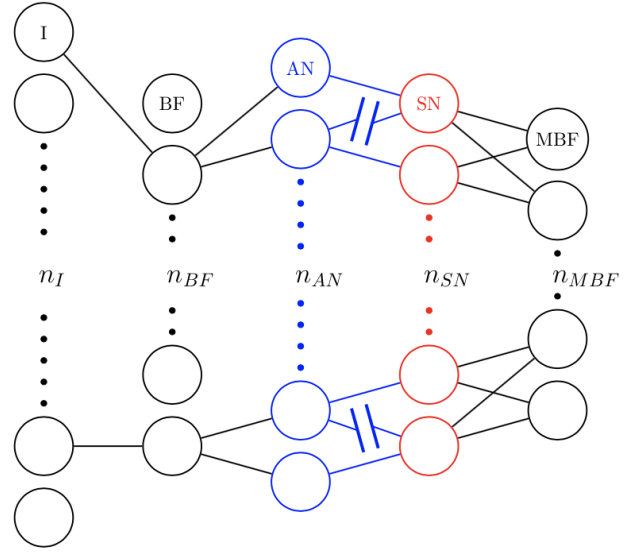


Fig. 2. Layers with conventional computational neurons, arithmetic and spiking neurons. Neuron numbers are indicated for the application case demonstrated in the subsequent section.

It occurred that if the arithmetic and SN layer are moved to the end of the stack, then features such as shorelines and highways are extracted. The output for this layer configuration is shown in Figure 6. The architecture and types of neuron layers utilized are listed in Table 2 below.

Table 2. Layer sizes

Layer	Task	Neurons	Appl. no.
1, input	spline input	$n_I = 3\ ev\ p$	11×10^{12}
2, normal	band fittings	$n_{BF} = 3\ ev\ r$	3×10^{11}
3, arithmetic	SN input	$n_{AN} = 3\ le\ v\ r$	6.2×10^{12}
4, spiking	extract error/feature	$n_{BN} = 3\ ev\ r$	3×10^{11}
5, normal	multiband fitting	$n_{MBF} = le\ v\ r$	10^{11}

3. APPLICATION

The bathymetry distributions obtained from satellite bands B_2 to B_4 and the final triband bathymetry distribution are shown in Figure 3 below. The triband bathymetry in the lower right corner exhibits a low error of 7.9% and high robustness as all pixels are successfully converted into bathymetric estimates. The method has been tested by applying it to recreational and residential artificial islands at the coast of Bahrain. The settled silt is visible on the uniformly dredged floor of the artificial island development. Depths at less than $2\ m$ are additionally error-prone due to tidal and wave dynamics. As the water column's relative transience is significant, the local reflectivity is increasingly ill-posed for extremely shallow sections. For example, in intertidal wet-dry zones and at centimeter scales the local relative error inherently spans the entire watercolumn.

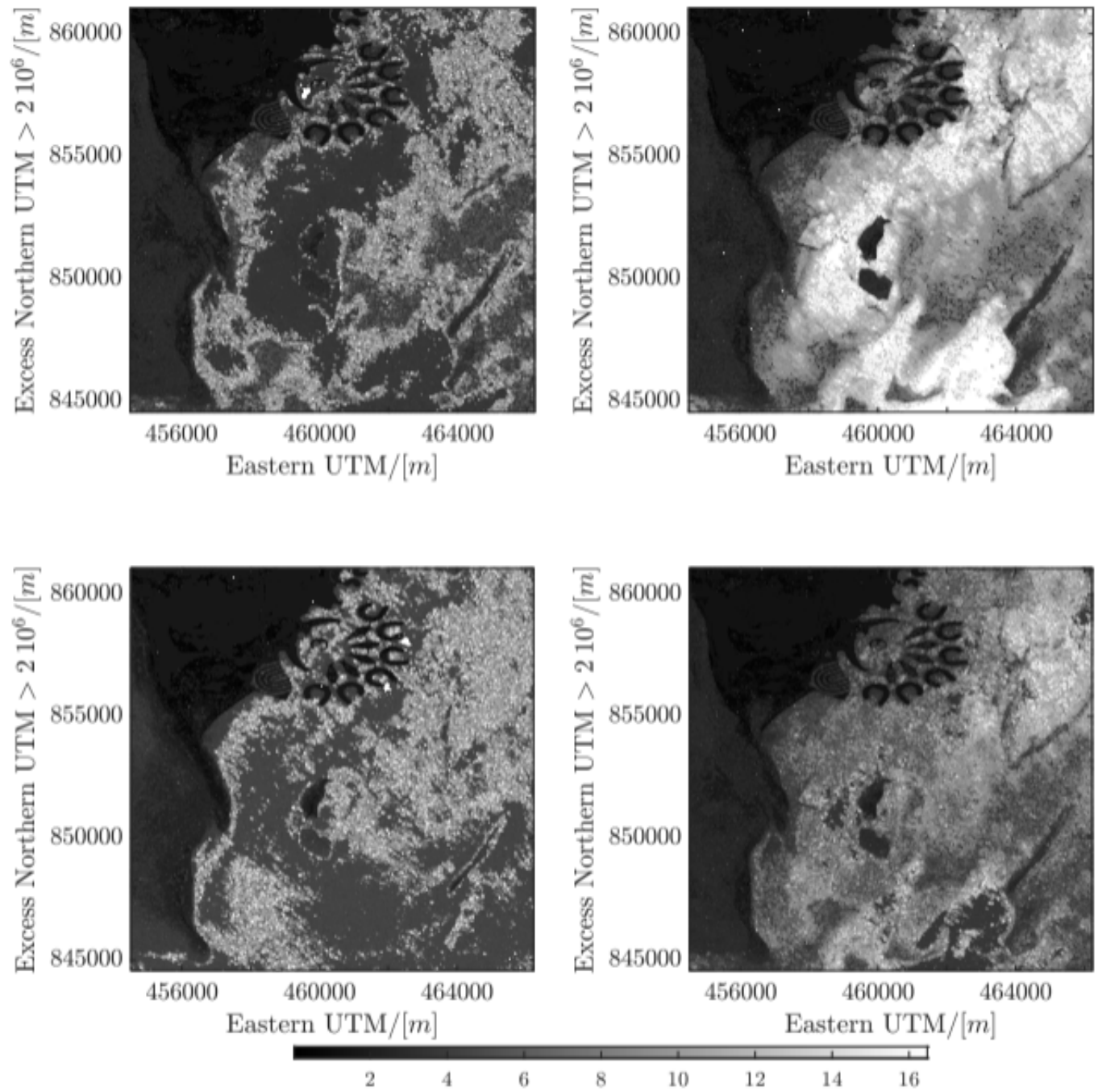


Fig. 3. Bathymetry sensing for band 2 (upper left), band 3 (upper right), band 4 (lower left), and a triband combination (lower right). The triband combination, shown in the lower right corner, is more robust and free of unrecognized swathes.

The accuracy has been assessed based on the average of all percent errors relative to soundings retained for error computation:

$$\text{error} = \frac{|d^m - d^{TB}|}{d^m} 100 \quad (11)$$

One third of the entire survey have been utilized for the error estimation. Each error is the normalized difference between the triband sensed depth d^{TB} and measurements d^m . The percent average errors are listed in Table 3 below.

Table 3. Percent average errors

	Band 2	Band 3	Band 4	Composite
Unfiltered	19.719	7.283	14.920	7.932
Filtered	19.608	7.081	14.696	7.917

The average error 7.9% for the filtered composite fitting translates to 0.21 m. Whereas the limited resolution of the Landsat satellite, that is, $30 \times 30 \text{ m}$, provides an inherent smoothing, high resolution commercial satellite images might benefit more from the SNN anomaly detection. The accuracy of the composite fitting is high enough to conduct a reliable automatic shoreline recognition with a sweeping algorithm. That is, the algorithm propagates from the deepest smoothed average and halts at pixels that are shallower than a cutoff depth. The dense infrastructure in artificial islands and streets in proximity to the shore required a deeper cutoff than natural shores. The filtered composite fitting with automatically excised land is depicted in Fig. 4.

An error distribution has been estimated by mapping the errors for certain depths to the best matching depths in Fig. 5.

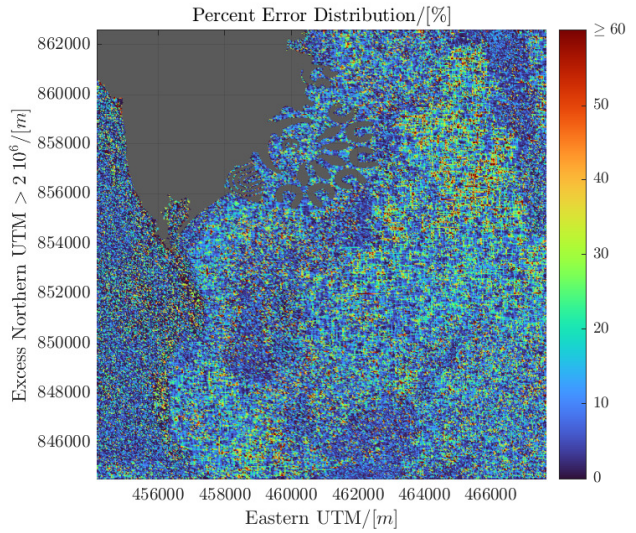


Fig. 5. Estimated error distribution.

4. CONCLUSION

The tri-band fitting, in conjunction with spiking neurons, permitted to sense bathymetry with an average percent error of 7.9 % or 21 cm. Stationary inputs can be processed by substituting time with spatial coordinates. The anomaly detection also underlined shorelines and roads, that is, object boundaries, as these are anomalies in terms of shading as shown in the appendix with Fig. 6. The remote sensing was accurate enough to automatically excise land from sea. That is, shoreline recognition is possible via both, vertical resolution or anomaly detection. Despite the low 30 m resolution of the Landsat image, improvements due to the anomaly detection were consistently found for all individual bands and the composite fitting. Gains are expected to increase for high resolution commercial satellite images and absent the inherent averaging of limited resolution.

Further investigations may include to detect anomalies in the sorted measurement series instead of vs. the seafloor and to smooth the weighting distribution beyond the current local weighting for each vertical increment.

Disclosures. The authors declare no conflicts of interest.

REFERENCES

1. E. C. Geyman and A. C. Maloof, "A Simple Method for Extracting Water Depth From Multispectral Satellite Imagery in Regions of Variable Bottom Type," *Earth Space Sci.* **6**, 527–537 (2019).
2. M. Al Najar, G. Thoumyre, E. W. J. Bergsma, R. Almar, R. Benshila, and D. G. Wilson, "Satellite derived bathymetry using deep learning," *Mach. Learn.* (2021).
3. G. Mandlbürger, M. Kölle, H. Nübel, and U. Soergel, "Bathynet: A deep neural network for water depth mapping from multispectral aerial images," *PFG – J. Photogramm. Remote. Sens. Geoinformation Sci.* **89**, 71–89 (2021).
4. A. M. Collins, K. L. Brodie, A. S. Bak, T. J. Hesser, M. W. Farthing, J. Lee, and J. W. Long, "Bathymetric inversion and uncertainty estimation from synthetic surf-zone imagery with machine learning," *Remote. Sens.* **12** (2020).

filteredvector-eps-converted-to.pdf

Fig. 4. SNN filtered bathymetry with automatically excised shoreline, exhibiting a common smooth area at the left and uneven areas in-front of the artificial islands.

5. "Anomaly detection in time series data using spiking neural network," Adv. Sci. Lett. **24** (2018).
6. S. J. Verzilizi, C. M. Vineyard, and J. B. Aimonel, "Neural-Inspired Anomaly Detection," Tech. Rep. SAND2018-5891C, Sandia National Laboratories (2018).
7. R. Al-Ruzouq and A. Shanableh, "Multi-temporal satellite imagery for urban expansion assessment at sharjah city /UAE," IOP Conf. Series: Earth Environ. Sci. **20**, 012010 (2014).
8. W. Cui, Z. Jia, X. Qin, J. Yang, and Y. Hu, "Multi-temporal satellite images change detection algorithm based on nsct," Procedia Eng. **24**, 252–256 (2011). International Conference on Advances in Engineering 2011.
9. "USGS Earth Explorer," Publisher: U.S. Department of the Interior.
10. R. A. Silver, "Neuronal arithmetic," Nat. Rev. Neurosci. **11**, 474–489 (2010).
11. I. Anderson, "Reviews - an introduction to the theory of numbers (sixth edition), by g. h. hardy and e. m. wright. pp. 620. 2008. (paperback). isbn: 978-0-19-921986-5 (oxford university press)." The Math. Gazette **94**, 184–184 (2010).

5. APPENDIX A

The anomaly detection correlates well with features such as shoreline and highways in Fig. 6 which constitute anomalies in shading. That is, constituting an SNN delineation of object boundaries. However, to aid road recognition, commercial satellite images with higher resolution than the Landsat images of 30 m would be required.

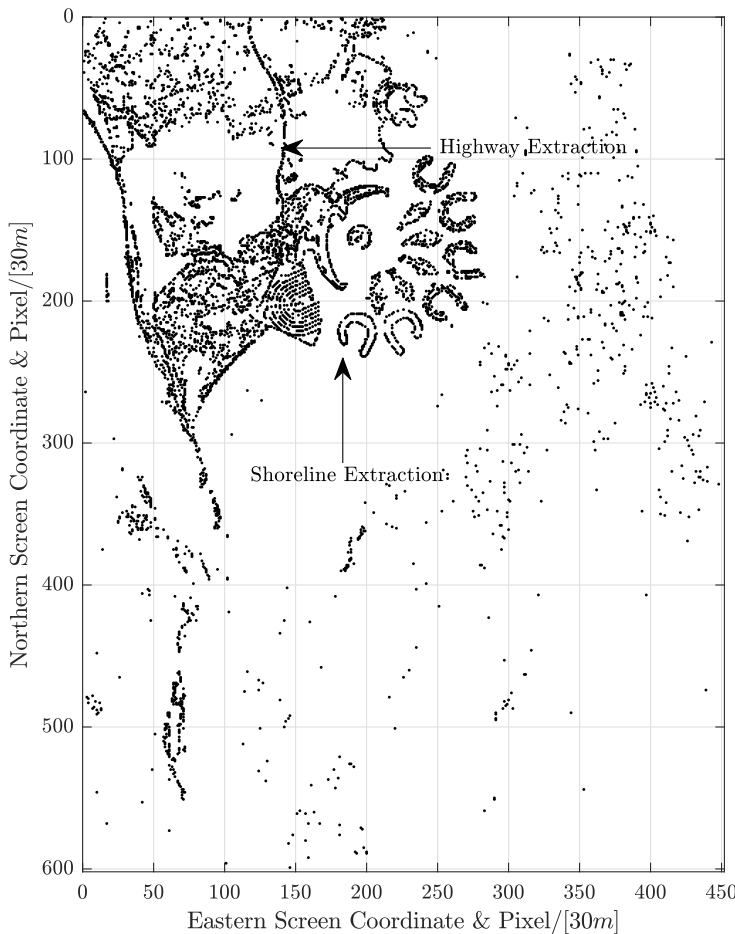


Fig. 6. Feature extraction despite limited 30 m resolution.

6. APPENDIX B

The code for the SNN is provided for at www.environment.report/code291121. This section provides a rigorous derivation of r_j with $r_j = \sqrt{a_j^2 + b_j^2}$. A pixel in \mathbb{R}^2 is a box B defined by $a_1, b_1, a_2, b_2 \in \mathbb{N}$ with the grid's centroids in intersection with the circle, yielding a sequence $r_i, i \in \mathbb{N}$ such that $C(\underbrace{0}_{\text{center}}, r_i)$:

$$B = \left\{ (x_1, x_2) : \begin{cases} a_1 \leq x_1 \leq b_1 \\ a_2 \leq x_2 \leq b_2 \end{cases} \right\}$$

The box's corners (a, b) in the image are vectors in the vector space $\mathbb{Z}^2 = \{(a, b) | a, b \in \mathbb{Z}\}$. Moreover, the distance from the corner to the center of the pixel is $\sqrt{a_j^2 + b_j^2}/2$.

Given the Fundamental theorem of arithmetic's [11] a integer $n > 1$ can be expressed as product of p_1, \dots, p_n primes s.t

$$n = p_1^{s_1} p_2^{s_2} \cdots p_k^{s_k}, s_i \in \mathbb{N}$$

Moreover, this representation is unique.

The sum of two squares theorem [11] states that an integer $n > 1$ can be written as a sum of two squares if and only if its prime decomposition contains no term p^k when $p \bmod 4 = 3$ and k is odd.

Subsequently the sequence radius r_i is derived. Every element, as per the above, given that r_i forms a monotonically increasing sequence. With each increment, the distance between the pixel of concern and a particular neighbor increases. Therefore,

(12)

$$i = p_1^{s_1} \cdot p_2^{s_2} \cdots p_k^{s_k} \text{ when } p_1, \dots, p_k \text{ are primes}$$

(13)

$$r_i = \left\{ \sqrt{i} : i = p_1^{s_1} \cdot p_2^{s_2} \cdots p_k^{s_k}, \nexists j : p_j \bmod 4 = 3 \wedge s_j \in 2\mathbb{N} + 1 \right\}$$

Determining existence on a particular circle for $n \in \mathbb{N}$ given with:

(14)

$$\left\{ \begin{array}{l} \text{On circle, } \phi > 0 \\ \text{Out circle, } \phi \leq 0 \end{array} \right\}, \phi = \sum_{\substack{d \mid n \\ d = 1, 3 \pmod{4}}} (-1)^{\frac{d-1}{2}}$$

The corresponding code is provided for at www.environment.report/code301121.